



OPEN ACCESS

EDITED BY

Lijie Guo,
Beijing Mining and Metallurgy
Technology Group Co., Ltd., China

REVIEWED BY

Lin Chi,
University of Shanghai for Science and
Technology, China
Shuhua Liu,
Wuhan University, China

*CORRESPONDENCE

Yongxiang Zhou,
✉ zhoux@bjut.edu.cn

RECEIVED 08 March 2023

ACCEPTED 06 April 2023

PUBLISHED 09 May 2023

CITATION

Wang C, Jing J, Qi Y, Zhou Y, Zhang K,
Zheng Y, Zhai Y and Liu F (2023), Basic
characteristics and environmental impact
of iron ore tailings.

Front. Earth Sci. 11:1181984.

doi: 10.3389/feart.2023.1181984

COPYRIGHT

© 2023 Wang, Jing, Qi, Zhou, Zhang,
Zheng, Zhai and Liu. This is an open-
access article distributed under the terms
of the [Creative Commons Attribution
License \(CC BY\)](https://creativecommons.org/licenses/by/4.0/). The use, distribution or
reproduction in other forums is
permitted, provided the original author(s)
and the copyright owner(s) are credited
and that the original publication in this
journal is cited, in accordance with
accepted academic practice. No use,
distribution or reproduction is permitted
which does not comply with these terms.

Basic characteristics and environmental impact of iron ore tailings

Changlong Wang¹, Jianlin Jing¹, Yang Qi¹, Yongxiang Zhou^{2*},
Kaifan Zhang¹, Yongchao Zheng³, Yuxin Zhai⁴ and Feng Liu⁵

¹Collaborative Innovation Center for Intelligent Regulation and Integrated Management of Water Resources Jointly Built by Provinces and Ministries, School of Civil Engineering, Hebei University of Engineering, Handan, China, ²Faculty of Architecture, Civil and Transportation Engineering, Beijing University of Technology, Beijing, China, ³State Key Laboratory of Solid Waste Reuse for Building Materials, Beijing Building Materials Academy of Science Research, Beijing, China, ⁴Technical Center, China Railway Construction Group Co., Ltd., Beijing, China, ⁵Construction Development Co., Ltd., China Railway Construction Group, Baoding, China

Introduction: In our study, various test methods were adopted to explore the mineralogical characteristics, grindability, particle morphology, particle size distribution, and environmental leaching toxicity of iron ore tailings (IOTs).

Methods: The methods include petrographic analysis, X-ray diffraction (XRD), scanning electronic microscopy (SEM), synchronous thermal analyzer (DSC-TGA), electron probe X-ray microanalyser (EPMA), and synthetic precipitation leaching Procedure (SPLP).

Results: The results show that the used IOTs contained 14.54% iron which was mainly stored in magnetite and pyrite. The content of iron silicate accounted for 11.82% of the total iron content. Most of it existed in silicate minerals, including grunerite and hornblende. A small amount of iron was contained in biotite, chlorite and augite. Besides, the grindability of IOTs was much better than that of granulated blast furnace slag (GBFS). After grinding for 140 min, the mass fraction of IOTs particles with the particle size less than 5 μm was 44.19%. These particles could be used to fill in the voids in the cement-powder-packed structure. IOTs also contained a large number of submicron and nanoscale particles.

Discussion: With great strength and environmental friendliness, the composite cementitious material (CCM) prepared from IOTs can be well applied to the building material field and environmental remediation.

KEYWORDS

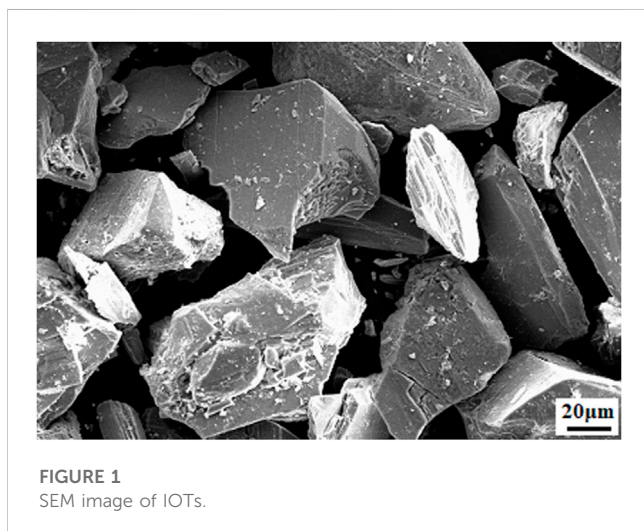
iron ore tailings (IOTs), mineralogical characteristics, grindability, Particle size distribution, particle morphology, composite cementitious material (CCM)

1 Introduction

Peak carbon dioxide emissions and carbon neutrality are the main development goals of all countries in the world (Nielsen et al., 2019; Yan et al., 2020). Cement manufacture, as one of the traditional industries with heavy energy consumption and emission, generates 5%–8% of the global CO₂ emissions per year (Turner and Collins, 2013; Mo et al., 2017). To save resources and reduce the emission of CO₂, various industrious solid wastes have been adopted to replace cement as the supplementary cementitious material, including granulated

TABLE 1 Particle size distribution of IOTs.

Sieve size/mm	+1.0	0.45–1.0	0.30–0.45	0.15–0.30	0.074–0.15	0.043–0.074	–0.043
Meter sieve/%	5.61	22.21	13.10	28.69	20.60	5.62	4.17
Cumulative sieve/%	5.61	27.82	40.92	69.61	90.21	95.83	100



blast furnace slag (GBFS) (Zhao et al., 2015), fly ash (FA) (Gunasekara et al., 2020), and silica fume (Campos Teixeira et al., 2020). Some researchers have founded that (Soliman and Nehdi, 2013; Ghafari et al., 2016; Meng and Khayat, 2018), adding appropriate amount of cementitious material can not only reduce the consumption of cement, but also improve the workability, mechanical properties, volume stability and durability of the concrete. With the wide application of the supplementary cementitious material (SCM) in the concrete industry, a large number of industrial by-products are rapidly consumed. To ensure the sustainable development of this industry, it is necessary to find SCM which are more accessible and more economical.

Iron ore tailings (IOTs) are the industrious solid waste discharged by concentrating mills after processing iron ores and selecting “valuable components” (Yao et al., 2020). In China, 600 million tons of IOTs are discharged every year and the IOTs deposition has reached 5 billion tons. However, the utilization efficiency across China is generally low, only 7% (Chen et al., 2021). In this case, large-scale harmless utilization of IOTs has attracted much attention. Currently, IOTs are mainly used for IOTs reclamation (Wang et al., 2018; Yuan et al., 2020; Yuan et al., 2020; Zhai et al., 2020) and mine filling (Onitiri and Akinlabi, 2017; Qiu et al., 2017; Coura et al., 2021), or used as the building material (Menders et al., 2019; Li et al., 2020; Zhang et al., 2022) and soil conditioner (Santana et al., 2020; Castro e Silva et al., 2021; Cui et al., 2021). IOTs are rich in SiO₂ and Al₂O₃ whose chemical composition is similar to that of cement (Han et al., 2017) and the physical properties are similar to those of natural sands (Huang et al., 2013). If IOTs can be adopted to prepare composite cementitious material (CCM), it will increase the utilization of IOTs, reduce its deposition, and lower the production cost, thus ensuring the

sustainable development of the concrete industry. IOTs can be used as the mineral admixture or alkali-activated cementitious material, and some can also replace ordinary Portland cement (OPC) (Zhao et al., 2014). Li et al. (2010) prepared CCM containing 30% clinker, 34% GBFS, 30% IOTs and 6% gypsum, whose mechanical properties are equivalent to OPC. Cheng et al. (2016) found that IOTs after mechanical activation had pozzolanic activity and could be used as SCM for concrete. Ling et al. (2021) used IOTs as the CCM to prepare environment friendly ultra-high performance concrete (UHPC), which facilitated the development of long-term compressive strength and the improvement of pore structure, thus ensuring the durability of UHPC. Cheng et al. (2020) prepared concrete with strong permeability resistance and good freeze-thaw resistance by replacing part of OPC with IOTs after mechanical grinding. The technology of preparing high-strength structural materials with IOTs has been studied in recent years. It aims to produce high value-added products from very fine-grained tailings. Zheng et al. (2010) reported that IOTs can be used to prepare high-strength structural materials with IOTs content of 70% and compressive strength of more than 100 MPa. For the high-strength structural material prepared with IOTs, superfine grinding technology was further required to process some ground IOTs, so as to generate some submicron and nanoscale IOTs particles. This process gives full play to the IOTs’ filling effect, bonding effect, and nanometer effect during the preparation of building materials. However, there are not many research results at home and abroad. In this case, fully utilizing the refinement effect of ground IOTs is of great importance to systematically study the physical and chemical characteristics and grindability of IOTs. Lawrence et al. (2003) found that inert quartz powder could facilitate the early hydration of OPC, because it could promote the process of heterogenous nucleation, and the finer the quartz powder, the more it attributed to heterogenous nucleation. Therefore, it is concluded that the incorporation of small amounts of low-activity ultrafine admixtures into UHPC has the potential to be an important means of improving concrete properties. Besides, for non-lime aerated concrete and foam cement products, it is also necessary to ultra-finely grind some siliceous raw materials to improve the pore structure of the products. Therefore, systematically exploring the physical and chemical characteristics, grindability and basic characteristics of very fine-grained IOTs after grinding is the basis for the overall utilization of such IOTs in the field of building materials.

To solve the above problems, X-ray diffraction (XRD), scanning electronic microscopy (SEM), synchronous thermal analyzer (DSC-TGA), and electron probe X-ray microanalyser (EPMA) were adopted to explore the mineralogical characteristics of IOTs, including the size composition, chemical composition, chemical phase composition, mineralogical phase composition, and microstructure. On this basis, SEM and particle size analysis were used to study the particle morphology and particle size distribution

TABLE 2 Chemical phase composition of IOTs (mass fraction, %).

Classification	Magnetite	Pyrrhotite	Carbonate iron	Sulfide iron	Hematite and limonite	Silicate iron	Total
Iron content	1.08	0.36	0.49	0.39	0.40	11.82	14.54
Iron distribution rate	7.43	2.48	3.37	2.68	2.75	81.29	100

TABLE 3 Radioactive test results of IOTs (mass fraction, %).

Sample	Specific activity of radionuclides (Bq·kg ⁻¹)			Internal exposure index	External exposure index	Test results
	²²⁶ Ra	²³² Th	⁴⁰ K			
IOTs				0.0	0.1	Qualified
	5.1	6.3	113.2			

Note: Internal exposure index = CRa/370 + CTh/260 + CK/4,200, external exposure index = CRa/200; uncertainty of measurement results (1σ) ≤20%.

TABLE 4 PDF card number and peak value corresponding to IOTs XRD pattern in Figure 3.

Mineral phase	PDF card number	2Theta
Quartz	46-1,045	20.7°, 26.6°, 40.2°, 59.8°, 68.3°
Plagioclase	09-0456	27.9°, 29.8°, 33.9°, 50.1°, 53.2°
Chlorite	29-0854	5.8°, 12.4°, 18.6°, 25.1°, 36.5°, 44.9°, 47.4°, 54.8°
Hornblende	23-1,046	28.5°, 29.1°, 38.4°, 45.7°
Calcite	72-1937	22.8°, 35.7°, 39.4°, 77.6°, 81.4°, 83.8°
Grunerite	17-1,622	9.7°, 32.3°, 55.3°, 66.6°, 67.7°, 75.6°, 79.8°
Biotite	80-1,106	19.5°, 21.9°, 27.2°, 34.6°, 42.3°, 61.4°
Augite	23-1,046	30.3°, 41.7°, 56.2°, 64.6°, 73.4°
Magnetite	88-0315	21.2°, 31.7°, 32.9°, 48.3°
Pyrite	29-0724	27.9°, 29.7°, 33.8°, 50.1°, 53.1°

characteristics of IOTs. Besides, specific surface area (SSA) was chosen as the evaluation index to compare the grindability of IOTs and GBFS. Finally, we adopted synthetic precipitation leaching procedure (SPLP) to test the leaching behavior of heavy metals in solidified body, so as to provide technical support for the utilization of IOTs.

2 Test materials and methods

2.1 Test materials

The IOTs used for our study was provided by Haoyang Mine Co., Ltd., in Ling Qiu county in Shanxi Province. The GBFS was offered by Qian'an Steel Co., Ltd., with the particle size of 0.30–2.5 mm and the grain size rate reaching 92.0%. For the 42.5 OPC, the initial setting time is 118 min and the final setting time 190 min, which meets the requirements of Chinese National Standard GB 175-2007 *Common Portland Cement*. Phosphogypsum (PG) is a kind of gray powder whose particle size is between 5 μm and 150 μm, density is 2.56 g·cm⁻³, and the SSA is 640 m²·kg⁻¹. The main mineral components are CaSO₄·2H₂O and CaSO₄·1/2H₂O.

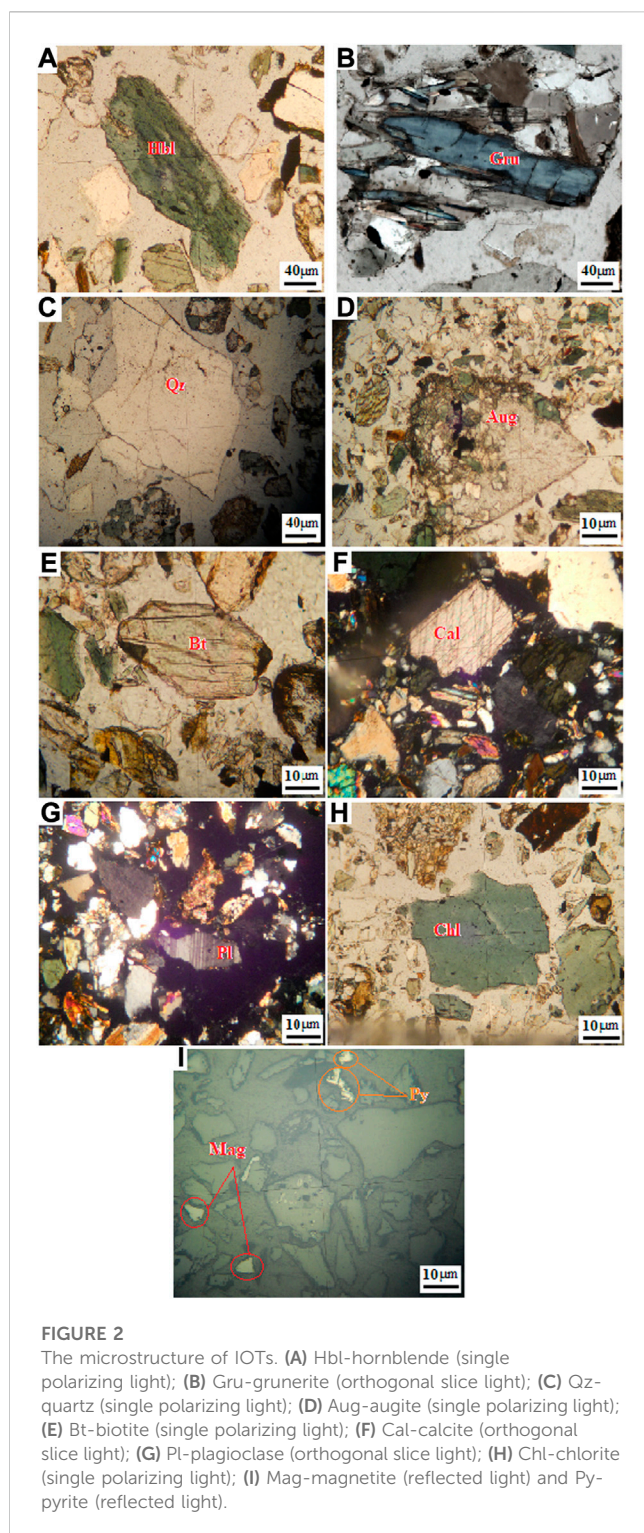
2.2 Test methods

2.2.1 Sampling method of raw materials

IOTs were taken from the middle of the IOTs pond by cutting the vertical section of the pit walls. The cutting depth was 1.2 m and the total weight of the samples was 640 kg. After mixed thoroughly, the samples were divided into 8 parts by the method of coning and quartering, and then sent back to the laboratory. Before the test, each pile of 80 kg IOTs was further divided into piles of 5 kg by the method of coning and quartering as the test samples.

2.2.2 Test of grinding characteristics

Firstly, IOTs and GBFS were dried in oven (CS101-3E) at 105°C for 24 h to make moisture content less than 1 wt%, and then ground with the SMΦ500 mm × 500 mm 5 kg small ball grinder (W·L⁻¹) at the speed of 48 r min⁻¹. The grinding media consisted of several steel balls and a steel forging. The loading mass of the grinding media should be 100 kg. The steel balls added up to 40 kg, in which the Φ70 mm balls took up 19.7%, the Φ60 mm balls 33.1%, the Φ50 mm balls 29.6%, and Φ40 mm balls 17.6%. The Φ25 mm × 30 mm steel forging weighed 40 kg. The grinding periods were chosen at 20 min, 40 min, 60 min, 80 min, 100 min, 120 min and 140 min in order to obtain different SSA.



2.3 Property characterizations

According to Chinese National Standard GB/T 19,077-2016 *Particle size analysis - Laser diffraction methods*, the particle size distribution of ground IOTs were analyzed through MASTER SIZER 2000 (a laser particle size analyzer with the analysis range of 0.02 μm –2,000.00 μm) with ethanol as the dispersant. The SSA of IOTs was measured by SSA-3200 (a dynamic specific surface area

analyzer). The XRD pattern was obtained by a D/Max-RC diffractometer (Japan) with Cu-K α radiation, voltage of 40 kV, current of 150 mA and 2θ scanning ranging between 10° and 90° . And the wavelength was 1.5406 nm. SEM observation was performed to analyse the mineral phase and the hydration products of the paste samples using a Zeiss SUPRATM55 scanning electron microscope coupled with a Be4-U92 energy spectrum. Leica DM4 P polarizing microscope was adopted for the petrographic analysis of IOTs. Netzsch STA 409 was used to heat the solidified powder from 25°C to $1,000^\circ\text{C}$ at the heating rate of $10^\circ\text{C}\cdot\text{min}^{-1}$ under N_2 , so as to explore the thermal decomposition rule of IOTs. IOTs were scanned with the JXA-8100 Electron probe microanalyzer (EPMA) to analyze the surface elements and their contents. SPLP was conducted to test the leaching behavior of heavy metals in solidified body, thus confirming the environmental safety. During SPLP, the leach liquor was prepared by adding 60%/40% (mass fraction) of sulfuric acid/nitric acid and diluting appropriately with deionized water, in order to adjust the pH to 4.20 ± 0.05 (Li and Chi, 2017). The leach liquor and solidified powder (0.075 mm) were mixed according to the ratio of 20:1, and shaken for 18 h in a gyrate shaker. Then, the screened mixture (0.45 μm) was put into Prodigy 7 Inductively coupled plasma emission spectrometer (ICP-OES) to analyze the concentration of Cr, Ni, Cu, Cd, Pb, Zn, As, and Hg (Zhu et al., 2017).

3 Results and discussion

3.1 Mineralogical properties of IOTs

3.1.1 Physicochemical properties of IOTs

The square hole screens with the screen size of 1.0 mm, 0.45 mm, 0.30 mm, 0.074 mm and 0.043 mm were used for the screen analysis of IOTs. The analysis results are displayed in Table 1. It can be seen that IOTs have large particle size, mainly between 0.074 mm and 1.0 mm. The grain size rate reaches 84.60%. Figure 1 shows that most of the IOTs are the particles with the size of tens of microns to hundreds of microns, and they are irregular or angular particles. As for the chemical composition of IOTs, inorganic components are the main content. The $\text{Fe}_2\text{O}_3+\text{FeO}$ content is 19.59% and total Fe (TFe) content reaches 14.54%, which exceeds the minimum grade of some iron ores mined in China. In the tailings, the content of SiO_2 is 54.41%, Al_2O_3 7.99%, $\text{CaO}+\text{MgO}$ 12.41%, and $\text{Na}_2\text{O}+\text{K}_2\text{O}$ 1.81%. For the harmful elements, S content is as high as 0.104% while P content is relatively low (0.052%). The contents of other harmful elements are small, too. Among the components of IOTs, the ratio of basic oxides to acid oxides is $(\text{CaO}+\text{MgO})/(\text{SiO}_2+\text{Al}_2\text{O}_3) = 0.199 < 0.5$, indicating that IOTs are acid tailings. To determine the occurrence state of iron in the samples, iron chemical phase analysis was conducted. The results are shown in Table 2. We can see that the iron in IOTs is mainly in the form of silicate iron and the distribution rate of iron is 81.29%. Then come the magnetite and carbonate with the iron distribution rate of 7.43% and 3.37%, respectively. In this case, the IOTs used for our study are the tailings with high silicate iron. The radioactivity index of the IOTs meets the requirement of Chinese National Standard GB/T 6566-2010 *Limits of radionuclides in building materials* (See Table 3).

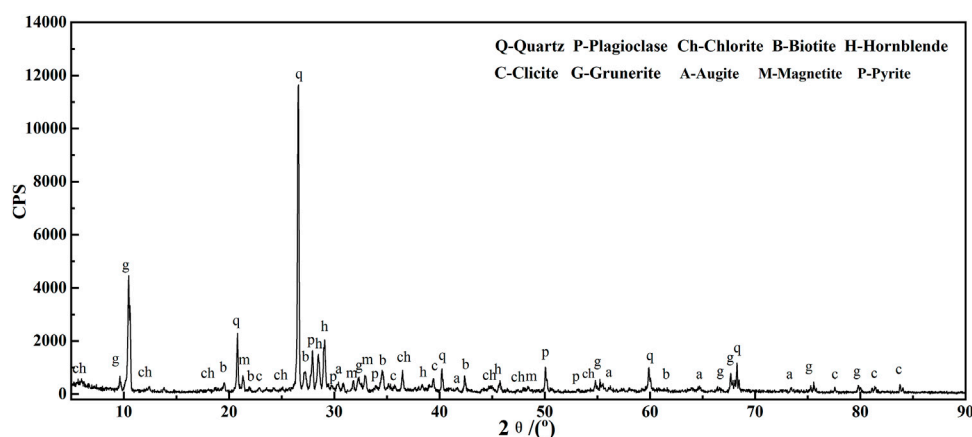


FIGURE 3
XRD pattern of IOTs.

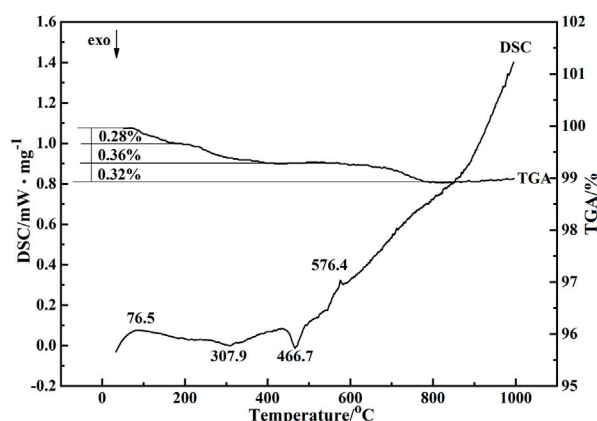


FIGURE 4
DSC-TGA curve of IOTs.

3.1.2 Structure and composition of IOTs

3.1.2.1 Petrographic analysis

To determine the material composition, structure, mineral composition, particle size, embedded features, and symbiotic relationship of IOTs, a polarizing microscope was used to observe the optical property differences of different minerals, thus identifying the minerals. The observed results are shown in Figure 2. From Figure 2, we can see that the metallic minerals identified in IOTs include pyrite and magnetite. There are 8 kinds of gangue minerals (high content: quartz, hornblende, grunerite, and plagioclase; low content: biotite, chlorite, calcite, and augite). Here are the characteristics:

Hornblende. With strong pleochroism and absorbency, it is one of the main rock-forming minerals in igneous rocks and metamorphic rocks. The color is dark green (Figure 2A).

Grunerite. It is a dark greenish-brown and columnar mineral with complete cleavage. It can turn into limonite and mainly exists in transmutative iron-bearing rock series (Figure 2B).

Quartz. It is one of the main rock-forming minerals. With the granular structure, it belongs to the stable mineral and is resistant to weathering (Figure 2C).

Augite. It is black green. See the two sets of pyroxene-type cleavage joints which are nearly orthorhombic in Figure 2D.

Biotite. It is in the form of pseudohexagonal plate and fully cleaved. It is brown with a slightly greenish tinge. There are opaque darkening edges around its phenocryst (Figure 2E).

Calcite. It has rhombic cleavage and paralleled twin striations. As the main mineral in calcareous rocks, it is widely distributed in sedimentary and metamorphic rocks (Figure 2F).

Plagioclase. With polysynthetic twin and complete cleavage, it is a tabular or columnar crystal (Figure 2G).

Chlorite. It has a layered structure with different shades of green. The color is getting darker with the increasing iron content (Figure 2H).

Magnetite and pyrite. With the cataclastic structure, they exist in the form of microgranular particles with the size of 3–4 μm (Figure 2I). They are filled with gangue minerals and are extremely refractory. Pyrite is pale yellow and it is a ubiquitous mineral that can occur in a variety of deposits. Magnetite is a brownish-gray mineral with no pleochroism.

3.1.2.2 XRD analysis

To determine the phase composition of IOTs, XRD was adopted to analyze the samples. The results are shown in Figure 3.

According to the XRD results in Figure 3, the main mineral components of IOTs are quartz, plagioclase, chlorite, biotite, hornblende, grunerite, augite, calcite, magnetite, and pyrite. The corresponding PDF card number and peak value are listed in Table 4. Based on the material balance principle (Huang et al., 2019; Ren et al., 2021; Yu et al., 2021), we used the linear programming program LINPRO (Faghihi et al., 2019; Bam et al., 2020) to calculate the content of each mineral phase: quartz (40%), hornblende (21%), grunerite (21%), plagioclase (9%), and others (9%). In hornblende ($\text{Al}_{3.2}\text{Ca}_{3.4}\text{Fe}_{4.02}\text{K}_{0.6}\text{Mg}_6\text{NaSi}_{12.8}\text{O}_{44}(\text{OH})_4$), the iron content is 12.73%, while the iron content is 39.03% in grunerite ($\text{Fe}_7\text{Si}_8\text{O}_{22}(\text{OH})_2$). Thus,

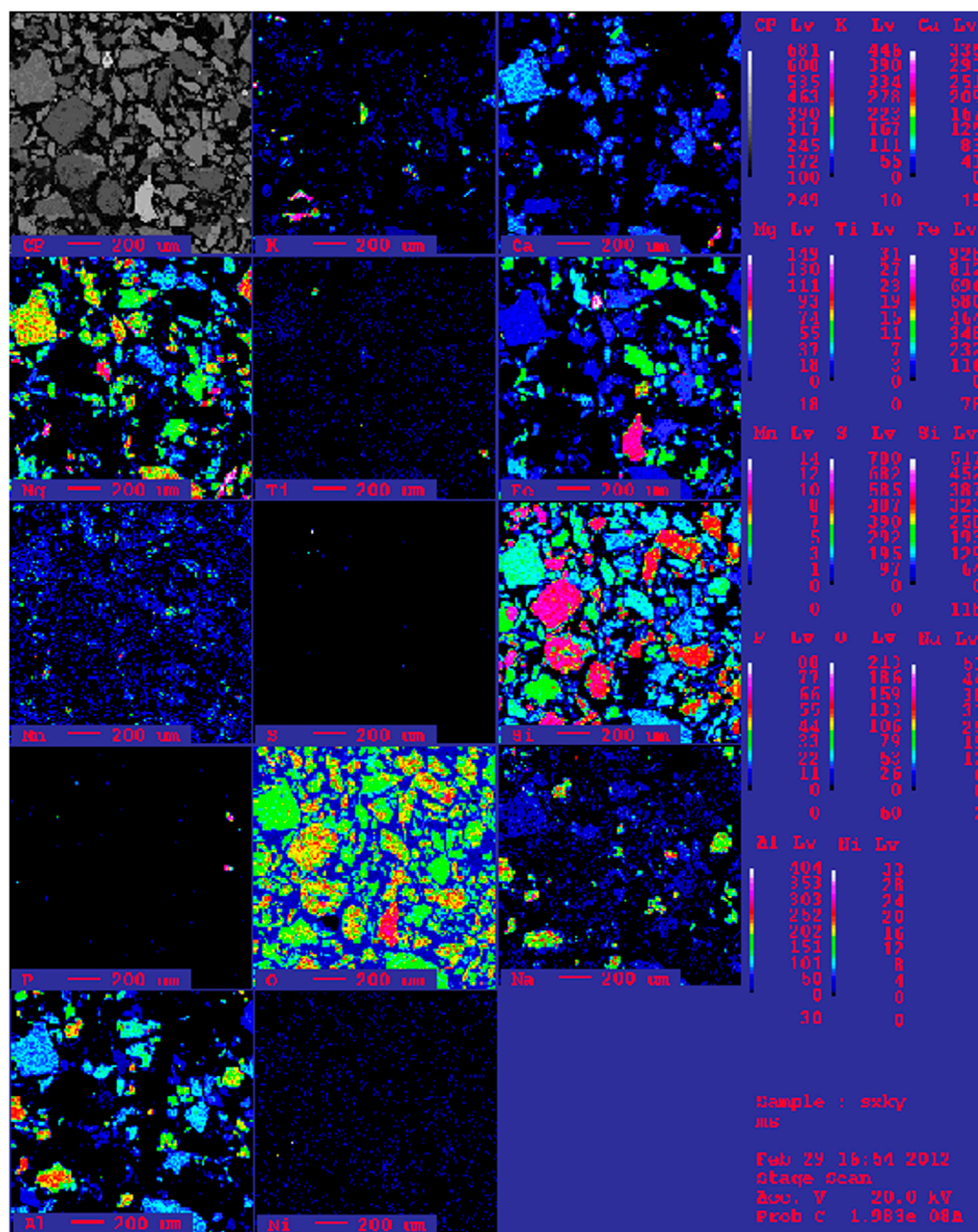


FIGURE 5 EPMA images of IOTs.

the total iron content of amphibole accounts for 10.87% of the IOTs. According to the chemical phase analysis results in Table 2, the content of silicate iron in IOTs is 11.82%, which indicates that most of the iron of IOTs exists in silicate mineral amphibole. Only a small amount of iron is contained in biotite, chlorite, and augite.

3.1.2.3 DSC-TGA analysis

Figure 4 is the DSC-TGA curve of IOTs. It can be seen that with the increase of temperature, the TGA curve shows a decline trend. It means that continuous weight loss occurs during the heating process

of IOTs, with a wide temperature range from 52°C (initial weight loss temperature) to 780°C (final weight loss temperature) and above. In the TGA curve, there are three obvious weight loss phases during the heating of IOTs.

In the first phase, the temperature range is 52°C–175°C and the weight loss rate is 0.28%. This phase mainly corresponds to the removal of the physically absorbed water in IOTs. Since the IOTs used for the analysis have been dried at 100°C, a large amount of water in IOTs has been removed. The endothermic peak of 76.5°C in this temperature range represents the removal of the remaining

TABLE 5 Quantitative analysis results of chemical elements detected by EPMA.

Chemical element	Mass ratio (%)	Atomic ratio (%)
Si	16.622	37.075
Ca	4.523	7.851
K	0.243	0.365
Na	0.921	2.558
Ni	0	0
S	0.239	0.341
Mg	4.256	16.36
Ti	0.099	0.121
Fe	8.937	16.112
Al	5.559	9.52
Mn	0.206	0.22
P	0.031	0.054
O	3.11	9.423
Total	44.746	100

physically adsorbed water. In the second phase, the temperature range is 175°C–400°C and the weight loss rate is 0.36%. A wide and flat exothermic peak appears at 307.9°C, mainly referring to the exothermic process of magnetite and pyrite at around 350°C. During this process, part of magnetite is oxidized to hematite and pyrite is oxidized to magnetite. In the third phase, the temperature range is 400°C–780°C and the weight loss rate is 0.32%. A sharp exothermic peak appears at 466.7°C while an endothermic peak occurs at 576.4°C. The exothermic peak mainly corresponds to the exothermic process where part of magnetite in IOTs is oxidized to hematite at the temperature between 400°C and 500°C. The endothermic peak refers to the endothermic process at the curie point temperature of magnetite (around 560°C) and the endothermic process where α -quartz in IOTs is transformed into β -quartz. The DSC-TGA analysis of the dried IOTs is basically similar to the iron phase analysis of IOTs.

3.1.2.4 EPMA analysis

Figure 5 shows the EPMA analysis results, including the distribution of K, Ca, Na, Mg, Ti, Fe, Al, Mn, S, Ni, P, and O. The element names are shown below each image. The scanning result of each element is represented with a colored tape, and the color density increases from bottom to top. In Figure 5, CP means the secondary electronic image.

Figure 5 shows that there is no Ni in the scanned area. The content of K is low, and most of it exists around the particles in the

lower left corner of the scanned area. In the scanned area, the Ca content is also low while the Na content is relatively high which is scattered in IOTs particles. The reason is that there are plagioclase-type minerals in IOTs (Figure 2G). Mg is concentrated near the middle of the scanned area. The content of Ti is not high. Fe is concentrated in two brighter regions in the CP secondary image, where the O content of larger particles is higher, indicating that they may be magnetite particles (Figure 2I). Al is distributed dispersively. However, the Al content is relatively higher in the particles containing Al and K. Mn and Ni are present in trace amounts in the scanned area, and the content of Mn is slightly higher than that of Ni. The Si content is high, and the color intensity is higher in the scanning area (red and pink). Considering the distribution of O, we can find that the scanned area has a high content of quartz (Figure 2C). The two harmful elements, P and S, are distributed sporadically in the scanned area and their contents are low. The quantitative analysis results of the elements in Table 5 also confirm the EPMA analysis results, which are similar to the analysis results in Table 6.

3.2 Grinding characteristics of IOTs

3.2.1 Grindability

The grinding energy consumption of GBFS is a well-known parameter in the field of building material. The energy consumption required for the one-time treatment of GBFS powder with the SSA of 400 m² kg⁻¹ or more is about 80 kW h t⁻¹ for a large industrial ball mill. However, that for the advanced vertical mill is 50–60 kW h t⁻¹. Therefore, in our test, the grindability of GBFS was used as a reference to study the grindability of IOTs. The IOTs and GBFS were ground in different batches by the SMΦ500 mm × 500 mm experimental ball mill, and we compared the difference in the SSA of their powder after grinding for the same time. Figure 6 shows the SSA of IOTs and GBFS at different grinding time.

It can be seen that the grindability of IOTs is much better than that of GBFS. Specifically, after grinding for 70 min, the SSA of GBFS is 400 m² kg⁻¹ while that of IOTs is 756 m² kg⁻¹. After grinding for 120 min, the SSA of GBFS is 515 m² kg⁻¹ while that of IOTs powder is 1,041 m² kg⁻¹. Besides, the SSA increase rate of IOTs is greater than that of GBFS. In other words, with the extension of grinding time, the SSA increment of IOTs is greater than that of GBFS. This is represented by the increasing slope of the curve of IOTs powder in Figure 6. It further confirms that IOTs have better grindability compared to GBFS.

Figure 7 shows the SEM images of IOTs and GBFS after grinding for 120 min. It can be directly seen that the fineness of IOTs at the same grinding time (Figure 7A) is much smaller than that of GBFS (Figure 7B). The SSA of IOTs after grinding for 120 min and 140 min are 1,041 m² kg⁻¹ and 1,059 m² kg⁻¹, respectively. Then, the SSA of IOTs remains relatively stable with the increase of grinding time. So it is of little significance to extend the grinding

TABLE 6 Chemical composition of IOTs (mass fraction, %).

Composition	SiO ₂	Al ₂ O ₃	Fe ₂ O ₃	FeO	MgO	CaO	Na ₂ O	K ₂ O	SO ₃	P ₂ O ₅	LOI
Content	54.41	7.99	8.94	10.65	5.85	6.56	1.18	0.63	0.26	0.12	3.41

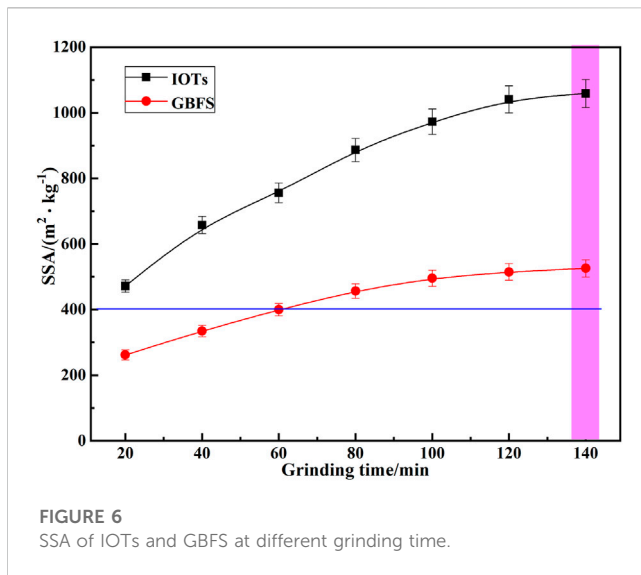


FIGURE 6
SSA of IOTs and GBFS at different grinding time.

time to improve the fineness of the powder after grinding for 140 min.

3.2.2 Particle size distribution of IOTs

A laser particle size analyzer (LPSA) was used to analyze the particle size distribution of IOTs at different grinding time. The results are shown in Table 7; Figure 8. It can be seen that with the extension of grinding time, the particle size distribution range of IOTs narrows and gradually concentrates towards the small particle size value. When the grinding time increases from 20 min to 140 min, D_{50} (median diameter) of IOTs powder decreased from 12.51 μm to 3.31 μm , and D_{90} decreased from 40.61 μm to 17.16 μm . D_{90} represents the particle size when the cumulative particle size distribution percentage reaches 90%. At the early stage of grinding, the particle size distribution of IOTs powder changed greatly. After grinding for 120 min, D_{50} and D_{90} only changed slightly with the increase of time, corresponding to the change of SSA.

In the concrete industry, mineral admixtures are an important component to improve the performance of concrete. Especially, they have better physical and chemical filling effects on cement-based

materials (Jindal, 2019; Sharma et al., 2022). The physical filling effect of mineral admixtures can effectively improve the compactness and fluidity of the fresh cement slurry, and reduce the porosity of the hardened slurry, thus improving its mechanical properties (Jiang et al., 2020; Ji et al., 2021). To give the full play of the physical filling effect, the mineral admixtures must have a suitable particle size and reasonable particle size distribution. Therefore, the core problem is to use the close packing principle of particles to obtain a dense filling structure of cement-based materials (Sun and Zhang, 2021; Wang et al., 2021). Chen et al. (2004) found that there are a large number of voids less than 5 μm in the cement powder packed structure, and adding into the powder with the particle size less than 5 μm could fill the voids among the cement particles, thus obtaining a closely packed structure. Figure 8 shows that, the particles with the size of less than 5 μm account for around 46.37% in the IOTs ground for 100 min, while those account for 51.75% in the IOTs ground for 140 min. With a great number of particles whose size is less than 5 μm , ground IOTs can be used to fill the voids in the cement powder packed structure, so as to make the structure more closed. The closely packed structure can reduce the water-cement ratio of the initial slurry, and significantly improve the mechanical properties and durability of the final cement-based materials (Lange et al., 1997; Peng et al., 2009). The reactive powder concrete with high strength and durability is also produced based on this principle (Richard and Cheyrezy, 1995). It can be expected that adding such inert particles can reduce water to a certain extent. The research team's previous research on using IOTs as mineral admixtures has shown that due to IOTs (Zhao et al., 2016; Wu et al., 2018). Most of the powder particles themselves exist in the form of polygonal irregular shapes. Compared to GBFS, the "interlocking function" between particles is stronger when they exist inside the mortar specimen. Under the standard curing conditions of high water binder ratio (0.48) and low water binder ratio (0.34) for 180 days, the main role of IOTs in the mortar blocks is the physical filling effect, regardless of the initial or late hydration period. No secondary hydration reaction of IOTs as mineral admixtures has been found. However, for the cementitious material products accepting high temperature steam or autoclave curing and mixed with ground IOTs, a large amount of crystalline silica in the IOTs can participate in the hydration reaction at a high temperature. In

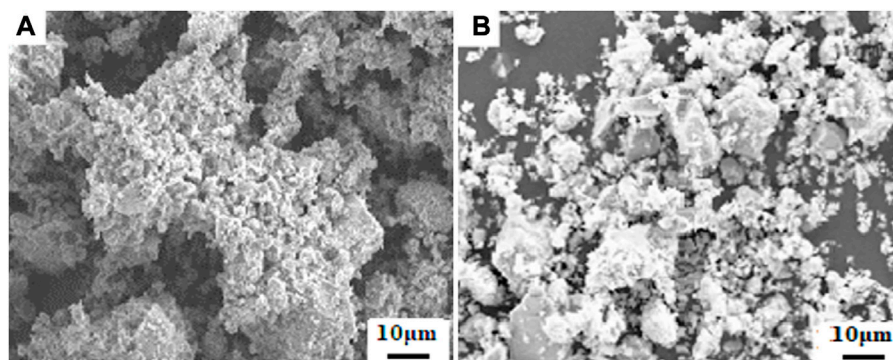


FIGURE 7
SEM images of IOTs and GBFS after grinding for 120 min (A) IOTs; (B) GBFS.

TABLE 7 Characteristic particle size of IOTs at different grinding time.

Grinding time/min	D ₅₀ /μm	D ₉₀ /μm
20	12.51	40.61
60	8.94	27.27
80	7.66	23.85
100	4.41	20.92
120	3.53	17.68
140	3.31	17.16

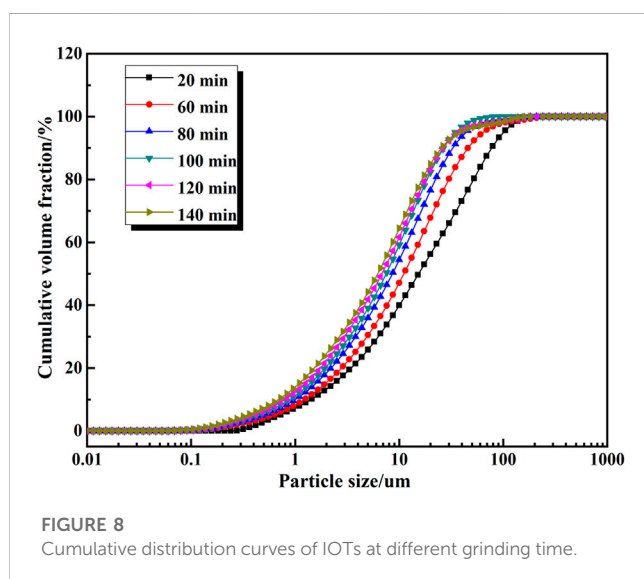


FIGURE 8 Cumulative distribution curves of IOTs at different grinding time.

this situation, the ground IOTs can not only realize physical filling, but also further exert its chemical filling effect. Meanwhile, Figure 6 shows that to obtain the GBFS with the SSA of 400–500 m² kg⁻¹ which is more widely used in the field of building material, the GBFS needs to be ground by an experimental ball mill for 90–120 min. However, at least 100 min is required to obtain the IOTs, 40% of whose particles have a size of less than 5 μm. It can be preliminarily predicted that when a large industrial mill is used, the energy consumption for grinding IOTs is close to that for grinding commonly used GBFS. This indicates that, in terms of technology requirement and energy consumption, it is feasible to apply the ground IOTs with a large number of ultrafine particles to the field of concrete.

Figure 9 shows microstructure and particle size distribution of IOTs at different grinding time. In Figure 9A, most of the coarse particles in IOTs ground for 20 min have irregular shapes. The size of some IOTs particles rapidly decreases to less than 5 μm after grinding, while some large particles are about 15 μm in size and they are mainly flaky and irregular polygonal blocks with sharp edges and corners. Figure 9B shows that after grinding for 60 min, the large particles in the IOTs are still clearly visible with the size reduced to about 10 μm. The edges and corners of the particles tend to be smooth, and the irregularity decreases. From Figure 9C, we can find that most of the IOTs particles after grinding for 100 min have the size of below 10 μm. The powder particles are significantly refined,

and a certain number of submicron particles less than 1 μm appear. Besides, they have arc-shaped edges, indicating the good sphericity. This shows that with the extension of grinding time, the sphericity of IOTs particles and the smoothness of the edges are both increased. In Figure 9D, flocculent weak agglomeration appears for the particles ground after 140 min. It can be clearly seen that nanoscale particles exist in the IOTs after ultrafine grinding. Their morphology tends to be spherical and the edges are smooth. With large surface energy, these nanoscale particles can agglomerate each other, or can be adsorbed on the surface of coarser particles. Therefore, ultrafine grinding of IOTs can not only generate a large number of submicron particles, but also obtain nanoscale particles with good sphericity. Figure 9E shows the particle size interval distribution curve of IOTs at different grinding time. As can be seen from the Figure 9E, as the grinding time progresses, the average particle size of IOTs also presents a regular decline with the change of grinding time. The range of particle sizes of IOTs with peak particle sizes gradually shifts towards fine particle sizes, while the peak particle sizes gradually decrease, gradually concentrating in the direction of small particle sizes, and the proportion of fine particle size components in the particle group gradually increases. After 20 min of grinding, the particle size decreases rapidly. With the extension of grinding time, the particle size of IOTs decreases gently. When grinding for 100–140 min, the particle size decreases slowly, indicating that there is a weak agglomeration phenomenon during mechanical grinding of IOTs. At this point, the weak bond is broken, making it more difficult for the stronger high-energy bond to break, increasing the fracture energy, and therefore reducing the grinding efficiency. This can also effectively illustrate the change rule in Figures 9A–D. The spherical shape of FA is one of the reasons why it plays an important role in the concrete industry. Adding spherical FA to concrete can effectively improve the fluidity of slurry, thereby improving the workability and mechanical properties of concrete. Therefore, when the IOTs after ultrafine grinding are applied as an inert filling component to concrete, the good particle sphericity will contribute to exerting the filling effect. In addition, with the rapid increase of lattice distortion and surface energy of some submicron and nano IOTs particles generated by grinding, the ground IOTs have certain volcanic ash reactivity. When they are applied as mineral admixtures to cement-concrete systems, these submicron and nanoparticles can undergo volcanic ash reaction, which will further improve the strength and durability of concrete (Cheng et al., 2020; Gunasekara et al., 2020; Ji et al., 2021).

3.3 Environmental impact of IOTs

At present, the application in the field of concrete is one of the focuses on IOTs research, while the leaching of heavy metals is still less concerned. As the iron and steel waste, IOTs contain heavy metals including Cr, Zn, Cu, Ni, Pb, Cd, Hg, and As (Zhang et al., 2018; Young et al., 2021; Sarathchandra et al., 2022), which are easy to migrate and transform in the environment. This poses a potential threat to the environment. In our test, SPLP was conducted to separately test the leaching toxicity of each raw material for preparing the CCM and that of the CCM hardened OPC paste. The raw materials included IOTs, OPC, and PG. The IOTs with the grinding time of 40 min and the SSA of 658 m² kg⁻¹ were assumed as

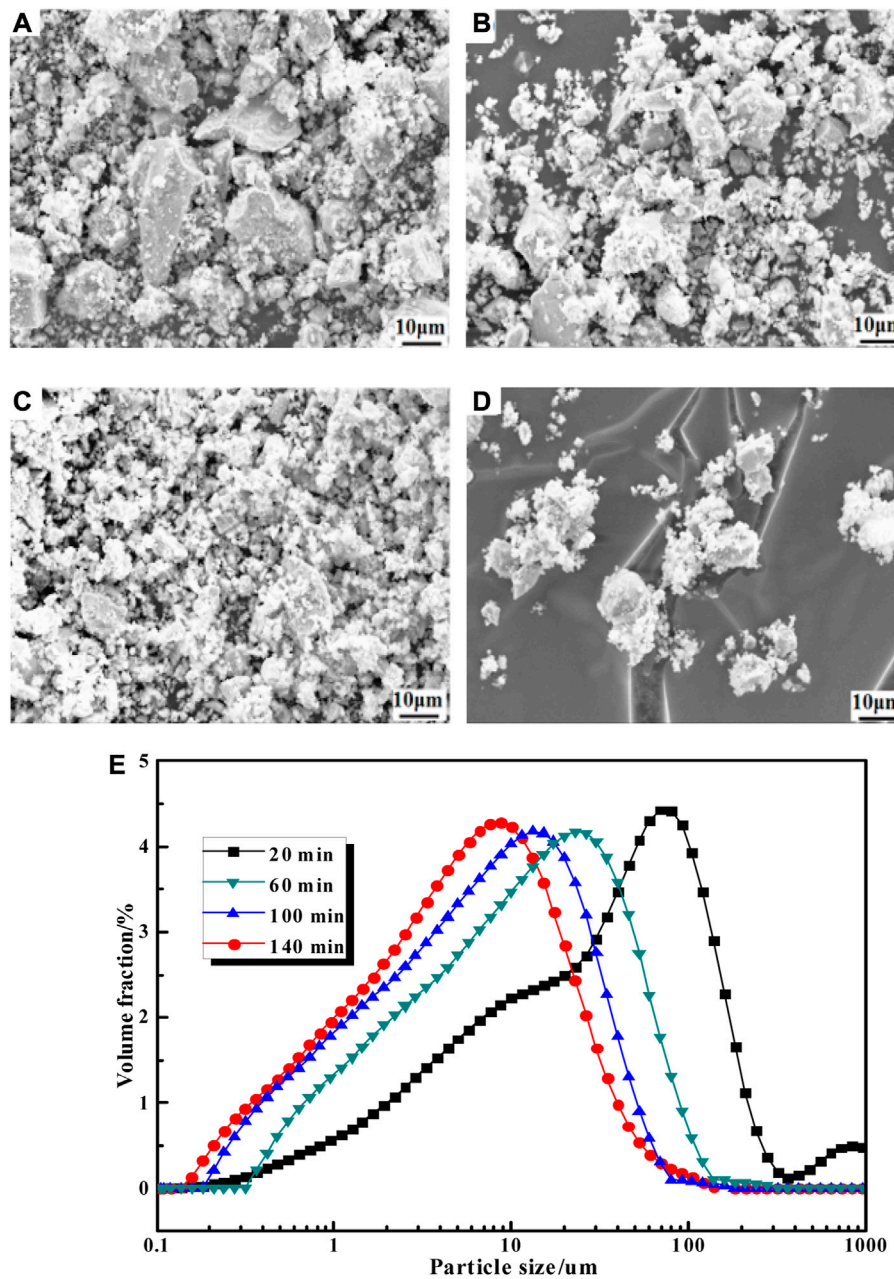


FIGURE 9 Microstructure and particle size distribution of IOTs at different grinding time. (A) 20 min; (B) 60 min; (C) 100 min; (D) 140 min and (E) Interval distribution curves.

TABLE 8 The leaching concentrations of heavy metals from some raw materials and mortar blocks of CCM after 28-day curing age (µg/L).

Materials	Cu	Pb	Zn	Ni	Cd	Cr	As	Hg
IOTs-1	18.42	0.77	54.47	0.6275	0.3641	0.793	2.1047	—
IOTs-2	20.23	0.92	72.14	1.1384	0.4818	0.964	2.9382	—
OPC	5.637	1.36	30.39	0.4538	0.5421	0.948	1.8525	0.04356
PG	26.161	0.16	37.71	0.0110	0.0908	1.176	0.6716	0.00224
CCM-1	12.368	0.52	33.93	0.5702	0.3518	0.684	1.3845	0.02711
CCM-2	16.581	0.84	46.82	0.9428	0.4903	0.825	1.6604	0.03326
Limiting value	100	5	100	5	1	5	5	0.1

IOTs-1. Those with the grinding time of 80 min and the SSA of $887 \text{ m}^2 \text{ kg}^{-1}$ were assumed as IOTs-2. The mix proportion of CCM was OPC: IOTs: PG=27:12:1. The CCM prepared with IOTs-1 was denoted as CCM-1, while that prepared with IOTs-2 was represented by CCM-2. The two kinds of CCM are the samples with better performance and more application value. The results are shown in Table 8. Although the leaching of heavy metals is detected from the raw materials in an acidic environment, the leaching concentrations are still far lower than the standard evaluation value stipulated in Chinese National Standard GB 5085.3-2007. In addition, the hydration and solidification of CCM can further reduce the risk of heavy metal leaching. Therefore, it is expected that even if IOTs are incorporated in the CCM system, the environmental risk coefficient of its application is still very low, compared to the limit value specified in Chinese National Standard GB 5085.3-2007.

4 Conclusion

This study systematically explores the physical and chemical properties, grindability, and basic characteristics of extremely fine particle iron ore tailings (IOTs), providing the basis for the comprehensive utilization of such IOTs in the field of building materials. The following conclusions are obtained:

- 1) The IOTs used for our study contain 14.54% iron and 54.41% SiO_2 . The main ferrous metal minerals are magnetite and pyrite. The content of silicate iron accounts for 11.82% of the total iron, most of which are found in silicate minerals, including grunerite and hornblende. A small amount of iron exists in minerals such as biotite, chlorite, and augite.
- 2) IOTs have good grindability which is much better than that of GBFS. After grinding for 120 min, the SSA of GBFS is $515 \text{ m}^2 \cdot \text{kg}^{-1}$ while that of IOTs powder reaches $1,041 \text{ m}^2 \cdot \text{kg}^{-1}$. From that time on, the SSA of IOTs basically remains stable even if the grinding time is extended.
- 3) The ultrafine grinding of IOTs can generate a lot of particles with the size of less than $5 \mu\text{m}$ which can fill in the voids in the cement powder packed structure. After grinding for 140 min, these particles account for 44.19% in the IOTs. The ultrafine grinding of IOTs can also generate submicron and nanoparticles with good sphericity. Therefore, IOTs after ultrafine grinding are expected to be applied to the cement-concrete industry, which is of great significance to improve the material property.
- 4) According to the environmental risk assessment, the CCM containing IOTs has low leaching toxicity. Its environmental risk coefficient is lower than the limit stipulated in Chinese National Standard GB5085.3-2007. Therefore, the CCM

containing IOTs have good application prospects in the field of building materials and environmental remediation.

Data availability statement

The original contributions presented in the study are included in the article/supplementary material, further inquiries can be directed to the corresponding author.

Author contributions

JJ proposes method and writes manuscript; CW and YXZ propose and participates in design research and reviews paper; YQ, KZ, YCZ, YuZ, and FL participate in design research and reviews paper. All the authors approved the final version of the manuscript.

Funding

The authors gratefully acknowledge financial support by the National Key Research and Development Program of China (No. 2021YFC1910605), the Natural Science Foundation of Hebei Province (E2020402079), State Key Laboratory of Solid Waste Resource Utilization and Energy Conservation (SWR-2023-007), Science and Technology Research and Development Plan of China Railway Construction Group Co., Ltd., (No. 22-11b, 22-14b), Handan Science and Technology Research and Development Program (21422111260). The funder was not involved in the study design, collection, analysis, interpretation of data, the writing of this article or the decision to submit it for publication.

Conflict of interest

Authors ZYu and LF were employed by China Railway Construction Group Co. Ltd, China.

The remaining authors declare that the research was conducted in the absence of any commercial or financial relationships that could be construed as a potential conflict of interest.

Publisher's note

All claims expressed in this article are solely those of the authors and do not necessarily represent those of their affiliated organizations, or those of the publisher, the editors and the reviewers. Any product that may be evaluated in this article, or claim that may be made by its manufacturer, is not guaranteed or endorsed by the publisher.

References

- Bam, L. C., Miller, J. A., and Backer, M. (2020). A Mineral X-ray linear attenuation coefficient tool (MXLAC) to assess mineralogical differentiation for X-ray computed tomography scanning. *Minerals* 10 (5), 441–455. doi:10.3390/min10050441
- Campos Teixeira, A. H., Soares Junior, P. R. R., Silva, T. H., Barreto, R. R., and Silva Bezerra, A. C. da. (2020). Low-carbon concrete based on binary biomass ash-silica fume binder to produce eco-friendly paving blocks. *Materials* 13 (7), 1534–1565. doi:10.3390/ma13071534

- Castro e Silva, H. L. C., Silva, A. M. L., Barros, R. M., Dos Santos, I. F. S., and de Freitas, J. V. R. (2021). Addition of iron ore tailings to increase the efficiency of anaerobic digestion of pig manure: A technical and economic analysis. *Biomass. Bioenerg.* 148, 1–18. doi:10.1016/j.biombioe.2021.106013
- Chen, G., Ji, G., Lei, A., and Tian, J. (2004). Study on synergistic effects of multi-component cementitious material. *J. Chin. Ceramic Soc.* 32 (3), 351–357. doi:10.3321/j.issn:0454-5648.2004.03.027
- Chen, T., Jian, S., Xie, X., Zhang, Y., Li, J., Li, B., et al. (2021). Research progress on comprehensive utilization of vanadium-titanium magnetite tailings. *Conserv. Util. Minerl. Res.* 41 (2), 174–178. doi:10.13779/j.cnki.issn1001-0076.2021.02.023
- Cheng, Y., Huang, F., Li, W., Liu, R., Li, G., and Wei, J. (2016). Test research on the effects of mechanochemically activated iron tailings on the compressive strength of concrete. *Constr. Build. Mat.* 118, 164–170. doi:10.1016/j.conbuildmat.2016.05.020
- Cheng, Y., Huang, F., Qi, S., Li, W., Liu, R., and Li, G. (2020). Durability of concrete incorporated with siliceous iron tailings. *Constr. Build. Mat.* 242, 118147–147. doi:10.1016/j.conbuildmat.2020.118147
- Coura, I. R., Carmignano, O. R. D. R., Heitmann, A. P., Lameiras, F. S., Lago, R. M., and Patricio, P. S. (2021). Use of iron mine tailing as fillers to polyethylene. *Sci. Rep.-UK* 11 (1), 7091–7099. doi:10.1038/s41598-021-86456-z
- Cui, X., Geng, Y., Li, T., Zhao, R., Li, X., and Cui, Z. (2021). Field application and effect evaluation of different iron tailings soil utilization technologies. *Resour. Conserv. Recy.* 173, 1–12. doi:10.1016/j.resconrec.2021.105746
- Faghihi, S., Keykhosravi, A., and Shahbazi, K. (2019). Modeling of kinetic adsorption of natural surfactants on sandstone minerals: Spotlight on accurate prediction and data evaluation. *Colloid. Interfac. Sci.* 33, 100208. doi:10.1016/j.colcom.2019.100208
- Ghafari, E., Ghahari, S. A., Costa, H., Julio, E., Portugal, A., and Duraes, L. (2016). Effect of supplementary cementitious materials on autogenous shrinkage of ultra-high performance concrete. *Constr. Build. Mat.* 127, 43–48. doi:10.1016/j.conbuildmat.2016.09.123
- Gunasekara, C., Zhou, Z., Law, D. W., Sofi, M., Sejeeva, S., and Mendis, P. (2020). Microstructure and strength development of quaternary blend high-volume fly ash concrete. *J. Mat. Sci.* 55 (15), 6441–6456. doi:10.1007/s10853-020-04473-1
- Han, F., Li, L., Song, S., and Liu, J. (2017). Early-age hydration characteristics of composite binder containing iron tailing powder. *Powder. Technol.* 315, 322–331. doi:10.1016/j.powtec.2017.04.022
- Huang, X., Fan, X., Chen, X., Gan, M., Ji, Z., and Zheng, R. (2019). A novel blending principle and optimization model for low-carbon and low-cost sintering in ironmaking process. *Powder. Technol.* 355, 629–636. doi:10.1016/j.powtec.2019.07.085
- Huang, X., Ranade, R., Ni, W., and Li, V. C. (2013). Development of green engineered cementitious composites using iron ore tailings as aggregates. *Constr. Build. Mat.* 44, 757–764. doi:10.1016/j.conbuildmat.2013.03.088
- Ji, G., Peng, X., Wang, S., Hu, C., Ran, P., Sun, K., et al. (2021). Influence of magnesium slag as a mineral admixture on the performance of concrete. *Constr. Build. Mat.* 295, 123619. doi:10.1016/j.conbuildmat.2021.123619
- Jiang, H., Fall, M., Yilmaz, E., Li, Y., and Yang, L. (2020). Effect of mineral admixtures on flow properties of fresh cemented paste backfill: Assessment of time dependency and thixotropy. *Powder. Technol.* 327, 258–266. doi:10.1016/j.powtec.2020.06.009
- Jindal, B. B. (2019). Investigations on the properties of geopolymer mortar and concrete with mineral admixtures: A review. *Constr. Build. Mat.* 227, 116644. doi:10.1016/j.conbuildmat.2019.08.025
- Lange, F., Mörtel, H., and Rudert, V. (1997). Dense packing of cement pastes and resulting consequences on mortar properties. *Cem. Concr. Res.* 27 (10), 1481–1488. doi:10.1016/S0008-8846(97)00189-0
- Lawrence, P., Cyr, M., and Ringot, E. (2003). Mineral admixtures in mortars: Effect of inert materials on short-term hydration. *Cem. Concr. Res.* 33 (12), 1939–1947. doi:10.1016/S0008-8846(03)00183-2
- Li, C., Sun, H., Bai, J., and Li, L. (2010). Innovative methodology for comprehensive utilization of iron ore tailings. *J. Hazard. Mat.* 174 (1-3), 71–77. doi:10.1016/j.jhazmat.2009.09.018
- Li, J., and Chi, S. (2017). Innovative solidification/stabilization of lead contaminated soil using incineration sewage sludge ash. *Chemosphere* 173, 143–152. doi:10.1016/j.chemosphere.2017.01.065
- Li, X., Wang, P., Qin, J., Liu, Y., Qu, Y., Liu, J., et al. (2020). Mechanical properties of sintered ceramsite from iron ore tailings affected by two-region structure. *Constr. Build. Mat.* 240, 117919. doi:10.1016/j.conbuildmat.2019.117919
- Ling, G., Shui, Z., Gao, X., Sun, T., Yu, R., and Li, S. (2021). Utilizing iron ore tailing as cementitious material for eco-friendly design of ultra-high performance concrete (UHPC). *Materials* 14 (8), 1829–1843. doi:10.3390/ma14081829
- Menders, B. C., Pedroti, L. G., Fontes, M. P. F., Ribeiro, J. C. L., Vieira, C. M. F., Pacheco, A. A., et al. (2019). Technical and environmental assessment of the incorporation of iron ore tailings in construction clay bricks. *Constr. Build. Mat.* 227, 1–13. doi:10.1016/j.conbuildmat.2019.08.050
- Meng, W., and Khayat, K. H. (2018). Effect of graphite nanoplatelets and carbon nanofibers on rheology, hydration, shrinkage, mechanical properties, and microstructure of UHPC. *Cem. Concr. Res.* 105, 64–71. doi:10.1016/j.cemconres.2018.01.001
- Mo, L. W., Zhang, F., Deng, M., Jin, F., Al-Tabbaa, A., and Wang, A. (2017). Accelerated carbonation and performance of concrete made with steel slag as binding materials and aggregates. *Cem. Concr. Comp.* 83, 138–145. doi:10.1016/j.cemconcomp.2017.07.018
- Nielsen, P., Boone, M. A., Horckmans, L., Snellings, R., and Quaghebeur, M. (2019). Accelerated carbonation of steel slag monoliths at low CO₂ pressure-microstructure and strength development. *J. CO₂ Util.* 36, 124–134. doi:10.1016/j.jcou.2019.10.022
- Onitiri, M. A., and Akinlabi, E. T. (2017). Effects of particle size and particle loading on the tensile properties of iron-ore-tailing-filled epoxy and polypropylene composites. *Mech. Compos. Mat.* 52 (6), 817–828. doi:10.1007/s11029-017-9633-4
- Peng, Y., Hu, S., and Ding, Q. (2009). Dense packing properties of mineral admixtures in cementitious material. *Particology* 7 (5), 399–402. doi:10.1016/j.partic.2009.06.003
- Qiu, J., Yang, L., Sun, X., Xing, J., and Li, S. (2017). Strength characteristics and failure mechanism of cemented super-fine unclassified tailings backfill. *Minerals* 58 (7), 58–13. doi:10.3390/min7040058
- Ren, S., Aldahri, T., Liu, W., and Liang, B. (2021). CO₂ mineral sequestration by using blast furnace slag: From batch to continuous experiments. *Energy* 214, 118975. doi:10.1016/j.energy.2020.118975
- Richard, P., and Cheyrezy, M. (1995). Composition of reactive powder concretes. *Cem. Concr. Res.* 25 (7), 1501–1511. doi:10.1016/0008-8846(95)00144-2
- Santana, P. H. L., Burak, D. L., Thiengo, C. C., Pecanha, A. L., Neves, M. A., and Mendonca, E. de S. (2020). Jack beans and vetiver grass growth on iron ore tailing sediments from the doce river dam disaster in Brazil: Plant growth regulator effects under different edaphic conditions. *J. Soil. Sediment.* 20 (2), 4103–4110. doi:10.1007/s11368-020-02774-1
- Sarathchandra, S. S., Rengel, Z., and Solaiman, Z. M. (2022). Remediation of heavy metal-contaminated iron ore tailings by applying compost and growing perennial ryegrass (*Lolium perenne* L.). *Chemosphere* 288, 132573. doi:10.1016/j.chemosphere.2021.132573
- Sharma, R., Jang, J. G., and Bansal, P. P. (2022). A comprehensive review on effects of mineral admixtures and fibers on engineering properties of ultra-high-performance concrete. *J. Build. Eng.* 45, 103314. doi:10.1016/j.jobee.2021.103314
- Soliman, A. M., and Nehdi, M. L. (2013). Effect of partially hydrated cementitious materials and superabsorbent polymer on early-age shrinkage of UHPC. *Constr. Build. Mat.* 41, 270–275. doi:10.1016/j.conbuildmat.2012.12.008
- Sun, J., and Zhang, P. (2021). Effects of different composite mineral admixtures on the early hydration and long-term properties of cement-based materials: A comparative study. *Constr. Build. Mat.* 294, 123547. doi:10.1016/j.conbuildmat.2021.123547
- Turner, L. K., and Collins, F. G. (2013). Carbon dioxide equivalent (CO₂-e) emissions: A comparison between geopolymer and OPC cement concrete. *Constr. Build. Mat.* 43, 125–130. doi:10.1016/j.conbuildmat.2013.01.023
- Wang, D., Ma, Y., Kang, M., Ju, Y., and Zeng, C. (2021). Durability of reactive powder concrete containing mineral admixtures in seawater erosion environment. *Constr. Build. Mat.* 306, 124863. doi:10.1016/j.conbuildmat.2021.124863
- Wang, W., Ye, P., Zhou, L., Wang, C., Huo, Z., Zhang, K., et al. (2018). Effects of reductant type on coal-based direct reduction of iron ore tailings. *Ann. Chim.-sci. Mat.* 42 (3), 453–466. doi:10.3166/acsm.42.453-466
- Wu, P. C., Wang, C. L., Zhang, Y. P., Chen, L., Qian, W., Liu, Z. Y., et al. (2018). Properties of cementitious composites containing active/inter mineral admixtures. *Pol. J. Environ. Stud.* 27 (3), 1323–1330. doi:10.15244/pjoes/76503
- Yan, W., Meng, Z., Zou, M., Miao, H., Ma, F., Yu, R., et al. (2020). Neutralization reaction in synthesis of carbon materials for supercapacitors. *Chem. Eng. J.* 381, 122547. doi:10.1016/j.cej.2019.122547
- Yao, G., Wang, Q., Su, Y., Wang, J., Qiu, J., and Lyu, X. J. (2020). Mechanical activation as an innovative approach for the preparation of pozzolan from iron ore tailings. *Min. Eng.* 145, 106068. doi:10.1016/j.mineng.2019.106068
- Young, G., Chen, Y., and Yang, M. (2021). Concentrations, distribution, and risk assessment of heavy metals in the iron tailings of Yeshan National Mine Park in Nanjing, China. *Chemosphere* 271, 129546. doi:10.1016/j.chemosphere.2021.129546
- Yu, J., Qin, Y., Gao, P., Han, Y., and Li, Y. (2021). An innovative approach for determining the grinding media system of ball mill based on grinding kinetics and linear superposition principle. *Powder. Technol.* 378, 172–181. doi:10.1016/j.powtec.2020.09.076

- Yuan, S., Zhang, Q., Yin, H., and Li, Y. (2020). Efficient iron recovery from iron tailings using advanced suspension reduction technology: A study of reaction kinetics, phase transformation, and structure evolution. *J. Hazard. Mat.* 404, 124067. doi:10.1016/j.jhazmat.2020.124067
- Yuan, S., Zhou, W., Han, Y., and Li, Y. (2020). Efficient enrichment of iron concentrate from iron tailings via suspension magnetization roasting and magnetic separation. *J. Mat. Cycles. Waste.* 22 (1), 1152–1162. doi:10.1007/s10163-020-01009-2
- Zhai, J., Wang, H., Pan, C., Hu, Y., and Sun, W. (2020). Recycling of iron and titanium resources from early tailings: From fundamental work to industrial application. *Chemosphere* 242, 1–8. doi:10.1016/j.chemosphere.2019.125178
- Zhang, X., Yang, H., and Cui, Z. (2018). Evaluation and analysis of soil migration and distribution characteristics of heavy metals in iron tailings. *J. Clean. Prod.* 172, 475–480. doi:10.1016/j.jclepro.2017.09.277
- Zhang, Y., Wang, L., Duan, Y., Liu, B., and Liang, J. (2022). Preparation and performance of Ce-doped far-infrared radiation ceramics by single iron ore tailings. *Ceram. Int.* 48 (8), 11709–11717. doi:10.1016/j.ceramint.2022.01.029
- Zhao, H., Sun, W., Wu, X., and Gao, B. (2015). The properties of the self-compacting concrete with fly ash and ground granulated blast furnace slag mineral admixtures. *J. Clean. Pr.* 95, 66–74. doi:10.1016/j.jclepro.2015.02.050
- Zhao, S., Fan, J., and Sun, W. (2014). Utilization of iron ore tailings as fine aggregate in ultra-high performance concrete. *Constr. Build. Mat.* 50, 540–548. doi:10.1016/j.conbuildmat.2013.10.019
- Zhao, X. M., Wang, C. L., Zheng, Y. C., Liu, S. C., and Yang, J. (2016). Properties of complex binder containing fly ash or iron ore tailings powder. *J. Chin. Coal Soc.* 41 (S1), 229–234. doi:10.13225/j.cnki.jccs.2015.1037
- Zheng, Y., Ni, W., Xu, L., Li, D., and Yang, H. (2010). Mechanochemical activation of iron ore tailings and preparation of high-strength construction materials. *J. Univ. Sci. Technol. B* 32 (4), 504–508. doi:10.13374/j.issn1001-053x.2010.04.016
- Zhu, X., Chen, B., Zhu, L., and Xing, B. (2017). Effects and mechanisms of biochar-microbe interactions in soil improvement and pollution remediation: A review. *Environ. Pollut.* 227, 98–115. doi:10.1016/j.envpol.2017.04.032